Proceedings of ASME Turbo Expo 2019: Turbomachinery Technical Conference and Exposition
GT2019
June 17-21, 2019, Phoenix, Arizona, USA

ASME Paper GT 2019-91776

FLOW MEASUREMENTS OF METHANE-FUELED ROTATING DETONATION COMBUSTION USING TIME-RESOLVED PARTICLE IMAGE VELOCIMETRY

Daniel L Depperschmidt, Jonathan R. Tobias, Robert S. Miller, Mruthunjaya Uddi, Ajay K Agrawal
Department of Mechanical Engineering
University of Alabama, Tuscaloosa, AL, USA

Jeffrey B. Stout
Aerojet Rocketdyne, Inc.
Canoga Park, CA, USA

ABSTRACT

Time-resolved particle image velocimetry (PIV) is applied to the flow field at the immediate exit of a rotating detonation combustor (RDC) operating on methane fuel and oxygen-enriched air. The detailed experimental results, which allow for the quantification of the periodic flow field, are believed to be the first such measurements acquired for a RDC. A thorough understanding of the velocity flow field exiting the combustor is important to develop future rotating detonation engine (RDE) design, as well as to successfully implement the flow conditioning devices to power generating turbine hardware located downstream. In this study, multiple PIV tests were conducted and a test case with over 16,000 consecutive image pairs acquired at a PIV framing rate of 30 kHz is analyzed in detail, and is supplemented with another test case to verify the repeatability of the measurements. Results are discretized into a two-dimensional flow field to reveal the significant insights to characterize the cyclical velocity fluctuations. While the flow field is primarily axial, a significant circumferential velocity component is also present. Key attributes of the velocity flow field are observed to be repeated from cycle-to-cycle. The codependency of the fluctuations in axial and circumferential velocity components are investigated, as is the relationship between velocity magnitude and flow orientation. At discrete measurement locations, the Fourier analysis of PIV data is used to reconstruct the cyclical variation of velocity components with respect to the phase angle.

INTRODUCTION

In recent years, pressure gain combustion (PGC) has received considerable attention in the scientific community because of its potential to increase the fuel efficiency [1-3]. One of the methods to utilize PGC is to replace deflagration with detonation in continuous flow, constant pressure systems such as gas turbines for power generation [4]. In this regard, pulse detonation combustion (PDC) has been studied extensively [5]. However, challenges such as intermittent operation requiring fast response inlet valves, inconsistent fuel-air mixing, low cycling frequency, etc., make it difficult to implement PDC in practical systems [6]. Rotating detonation combustion (RDC) is an alternative approach whereby detonation occurs in the circumferential rather than the linear direction used for PGC. Thus, RDC yields a continuous combustion process, and although first conceived by Voitsekhovskii [7] and Nicholls [8] in 1960's, the concept has been vigorously investigated in recent years because of its potential to increase the fuel efficiency. Hardware implementing RDC is referred to as the rotating detonation engine (RDE), and the two terms, RDC and RDE, are often used interchangeably. Studies of RDC employ axial flow between circular channels such as an annulus, radial flow between circular disks or even flow in a circular pipe to achieve continuous rotating detonation [9-11]. Figure 1 illustrates the important physical processes in RDC representing the annular hardware employed for the present study.

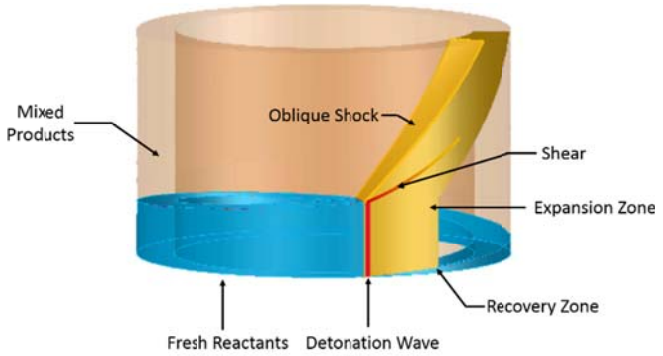

FIGURE 1. ILLUSTRATION OF ROTATING DETONATION COMBUSTOR.

Reactants are fed axially at the bottom of the annulus at elevated pressures through separate fuel and oxidizer plenums located upstream of the combustor annulus. Vigorous fuel-air mixing occurs at the base of the annulus, and then the reactants are consumed by the detonation wave(s) propagating in the circumferential direction, effectively chasing the supply of fresh reactants. The pressure (and temperature) increases rapidly across the detonation wave, and subsequently, the detonation products turn towards the axial direction as they expand across an oblique shock wave riding above the detonation wave. Injection plates downstream of the fuel and oxidizer plenums are often of complex design to promote proper mixing. Flow rates of reactants, and therefore of the subsequent products and generated thrust, are functions of the inlet pressure of the reactants. The means of controlled injection therefore does not require complex valve devices or mechanisms.

The detonation wave speed depends upon fuel and oxidizer types, reactant flow rate, equivalence ratio, etc., and it can easily exceed 2000 m/s (or several thousand rotations per second), thereby appearing as continuous combustion although, in principle, the detonation is intermittent relative to a stationary reference frame. Multiple detonation waves of self-similar or even opposing orientation (often referred to as a "slapping mode") have been observed [12-13]. Many studies have been conducted to understand the operating principles and important physical mechanisms of RDC in an effort to optimize it for practical applications [14-17]. Several researchers have performed extensive experimental investigations of RDC including parametric studies for a range of operating conditions and with various diagnostic techniques [17-25]. For example, Rankin *et al*. [25] were the first to use OH* chemiluminescence to visualize and characterize detonation within the annulus. The details of the dynamic coupling between the detonation wave and the fuel plenum have been investigated using Schlieren imaging [22]. Rankin *et al*. [23] conducted studies of RDC with an integrated downstream nozzle and found that the nozzle was effective in reducing the periodicity of the RDC exit flow. Performance based studies have been conducted by Sousa et al. [4] and Kawalec and Wolanski [26-27] among others.

RDC computational studies often focus on characterization of losses associated with high pressure injection systems, and the propagation of detonation and oblique shocks waves in the RDC annulus. Schwer and Kailsanath [28] developed a numerical method to model the RDC flow field and identified potential losses caused by imperfect detonation and propagation of shock wave(s) in the products. Paxson [29] created a simplified 2D model of RDC with a coarse grid to reduce the computational cost while still achieving reasonable agreement with more complex simulations. A reduced-order model of the thermodynamic cycle of RDE was developed by Kaemming et al. [30] to provide a closer inspection of loss mechanisms such as imperfect detonation and varied injection area.

Kailasanath and Schwer [31] used high fidelity 3D simulations to characterize the flow field associated with a RDE and to identify the key parameters that affect RDE performance. They noted that the flow field exiting into a plenum from a RDE annulus without a centerbody or aerospike had small radial velocities in addition to axial and azimuthal flow components. Nordeen *et al*. [32] modeled the RDE flow field, and compared the flow behavior through multiple configurations of attached flow conditioning devices. The study detailed the non-axial flow component referred to as the "swirl" resulting from the acceleration by the azimuthal pressure gradient, and identified two flow zones with opposing swirl. As a result, the exhaust flow of a typical annular RDE exhibited a reversal of swirl twice per revolution of a single detonation wave, denoted as "positive and negative swirl". Nordeen *et al*. [32] showed that, in agreement with the conservation of momentum, the mass averaged flow in the azimuthal direction was nearly zero, and that the azimuthal flow fluctuations were attenuated by a diffuser-like assembly including a converging-diverging (CD) nozzle. Because the azimuthal (or circumferential) velocity component is not continuous around the RDE periphery, it will be referred to as "tilt" rather than "swirl" in this study.

The present study is motivated by two significant and important objectives to advance the fundamental understanding of RDC and related processes. First, the majority of the previous studies were inspired by RDC's potential for thrust augmentation realized by pressure gain. These studies have most commonly utilized hydrogen fuel. RDC could also replace the conventional combustion system in power generating gas turbines. Pressure gain in RDC will increase the combustor exit (or turbine inlet) pressure, thereby increasing the thermodynamic cycle efficiency. In this application, natural gas (or methane as the major component) is the fuel of choice. However, methane is difficult to detonate, and as such, few studies of RDC with methane have been performed in the past [11]. The research team at The University of Alabama (UA) is engaged in RDC research for power generation using methane fuel [33-35], and this is also the focus of the present study.

Second, the cyclic nature of rotating detonation results in periodic pressure and thus, flow oscillations in the combustion products that must be satisfactorily attenuated upstream of the turbine inlet without incurring significant losses. Of particular interest is the combustor flow field, and periodic oscillations therein, to develop strategies to efficiently condition the flow between RDC and turbine inlet.

Past studies have used high-speed imaging to qualitatively assess the unsteady flow field of a RDE. For example, Nordeen [36] used high-speed imaging to depict the oscillatory behavior of the non-axial component of a RDE exhaust plume. However, to the best of our knowledge, detailed experimental flow measurements within or outside the RDC have not been

obtained so far. The present study overcomes this drawback by acquiring velocity measurements at the RDC exit by employing the time-resolved particle image velocimetry (TR-PIV) whereby a high-speed imaging system is used to track small seed particles introduced in the flow as they traverse through a planar laser sheet [37-39]. The measurements obtained in this study are intended to assist in the development of flow conditioning devices, to help validate high-fidelity computational models, and to quantify the pressure gain realized in RDC systems, in conjunction with other scalar field measurements.

However, there are many challenges associated with obtaining reliable TR-PIV measurements in reacting, supersonic, highly periodic flows. The choice of materials for seed particles is limited owning to the extreme temperature and pressure conditions associated with supersonic combustion processes. High velocity, intermittent supply of fuel and oxidizer from small injection holes and safety concerns associated with foreign particles in high purity oxygen line(s) place severe constraints on how and where the seed is introduced. Additionally, in supersonic, compressible flows, the velocity changes dramatically across the shock and/or expansion waves. The associated flow acceleration or deceleration can lead to inconsistent seed distribution, severe seed agglomeration, and significant relative motion between seed particles and the surrounding fluid flow depending upon the seed relaxation time [40-41]. Ragni *et al*. [40] conducted experiments in conjunction with numerical simulations to test and validate the response time of selected metallic ceramic seed compounds across a fixed oblique shock. Haghdoost *et al*. [41] conducted a similar study and found results in agreement with Ragni *et al.* [40]. Small seed particles are needed to reduce the relaxation time, but small particles also scatter much less light. Thus, the laser intensity in the PIV field of view must be very high, which is limited by the available laser power at high pulse rates.

There are few studies of PIV measurements in supersonic flows with combustion [42-43]. However, to the best of our knowledge, no previous study has been conducted on the high cyclic frequency (>6000 Hz), time-dependent periodic flow of RDC exhaust. Thus, in this study, many of the experimental challenges associated with TR-PIV were addressed to gain insight into the oscillatory flow field at the RDC exit. It is intended that this study will be an important step forward to help realize diagnostics refinements in the future and to improve the physical understanding of RDC flow field.

EXPERIMENTAL SETUP

Figure 2(a) displays a photograph of the RDE located in a test cell at the Engine and Combustion Laboratory (ECL) at UA. A bisectional diagram profiling the RDE is presented in Fig. 2(b). The modular design of the combustor, developed by Aerojet Rocketdyne consists of three concentric spools stacked together and a circular center-body which extends beyond the annulus into an aerospike configuration. The combustion annulus has an outer diameter of 10.0 cm and an inner diameter of 8.0 cm. In this study, the RDC was operated at a high pressure to replicate conditions in a realistic gas turbine combustor. Thus, an additional spool with a CD nozzle to simulate the back pressure was attached downstream of the

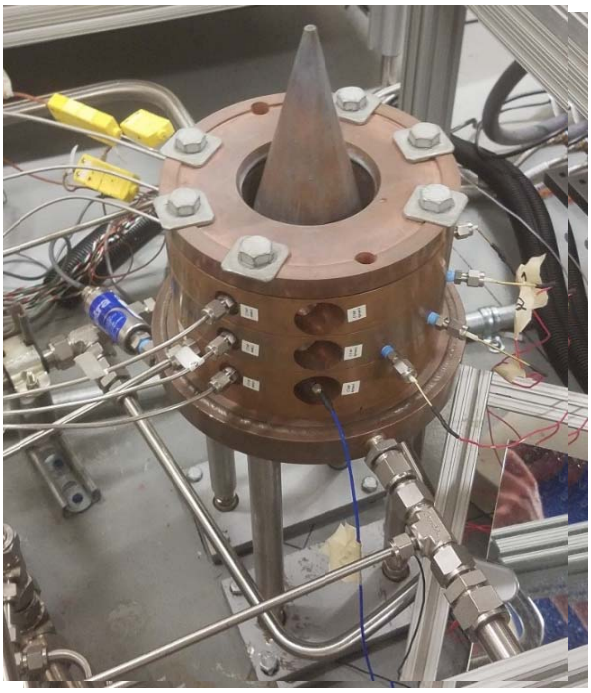

Figure 2(a). PHOTOGRAPH OF THE RDE AT THE UNIVERSITY OF ALABAMA.

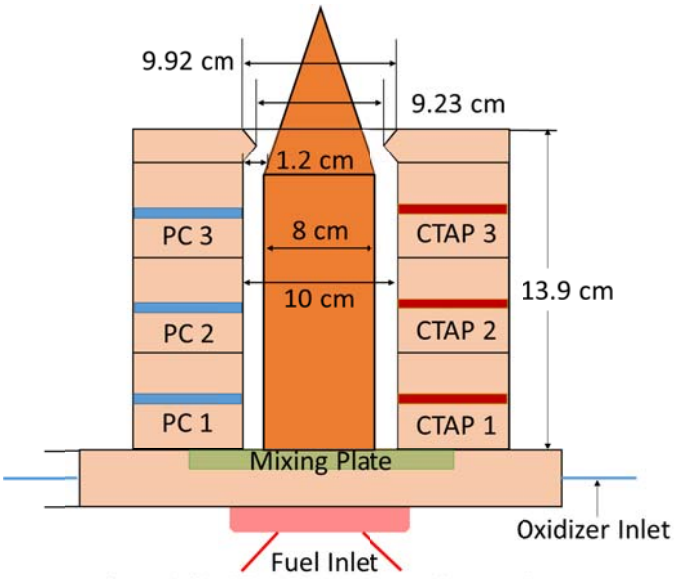

Figure 2(b). SCHEMATIC DIAGRAM OF THE ROTATING DETONATION COMBUSTOR

third spool of the RDC. The back-pressure CD nozzle consists of 32 degree convergence and 25 degree divergence sections, providing contraction area ratio of 1.39 and expansion area ratio of 1.55. The aerospike diameter is constant (8 cm) along the length of the back-pressure nozzle, intended to restrict the flow, and hence, to operate the RDC at elevated pressures. The chamber spools and any part subject to high heat flux is made of pure oxygen-free high conductivity (OFHC) copper. Other parts such as the manifold assembly are made from copper-chromium alloy (CuCr C18200), which has about 1-2% chrome to reduce the thermal conductivity to about 77% of OFHC while increasing yield and ultimate strengths. Figure 2(b) also

shows the locations of static pressure probes denoted as PC (pressure capillary) and CTAP (capillary tube average pressure).

The RDE is operated with methane fuel and oxygen-enriched air as the oxidizer. Each reactant gas supply system (methane, air, and oxygen) consists of storage gas cylinder racks, sonic nozzle instrumented with pressure and temperature transducers to measure the mass flow rate, and an electro-pneumatic valve adjacent to the RDE to quickly turn on/off the flow. Air and oxygen lines combine to form the oxidizer line, and subsequently fuel and oxidizer lines feed into the respective plenum chambers located at the base of the RDE. RDE operation is initialized by igniting a hydrogen-oxygen mixture in a separate line, and introducing the resultant detonation wave radially into the RDE. The RDE is oriented vertically within a Lexan enclosure, and the test cell is equipped with supply of ventilation and exhaust air to safely release the combustion products to the atmosphere.

The operation and timing of the experiment are precisely controlled by an in-house developed control system using multiple BeagleBone microprocessors to prevent deflagration combustion at the start of the RDE. Further details of the test facility, instrumentation, and operation are given in recent publications by Welch *et al.* [33] and Tobias *et al.* [34]. The remainder of this section will focus on experimental details pertinent to the successful application of TR-PIV to characterize the flow field at the RDE exit. Besides providing important physical insight into the RDE exit flow field, the results presented herein will be an important step to eventually acquire similar measurements inside the RDE operating at high pressures.

Figure 3(a) depicts the flow system designed to deliver the seed particles to the RDE. Details of the seeder design are shown in Figure 3(b). High pressure air flow from a compressed gas cylinder is measured by a sonic nozzle, and then delivered to the seeder. The air supply pressure is controlled by a pressure regulator, and the airflow rate through the seeder is measured by pressure and temperature transducers located across a sonic nozzle. The seeder can be bypassed from the flow system by a three-way manual valve. Seed particles placed on a fine stainless steel mesh within the seeder are entrained by the swirling airflow, and then the seeded flow exits from the top. A non-critical venturi is located downstream of the seeder to accelerate the flow and thus, break up agglomerated seed prior to the seeded flow merging with the primary oxidizer flow. The seeded flow mixes with the primary oxidizer flow and then, the seeded oxidizer flow enters the combustor annulus through the oxidizer manifold and injection plate.

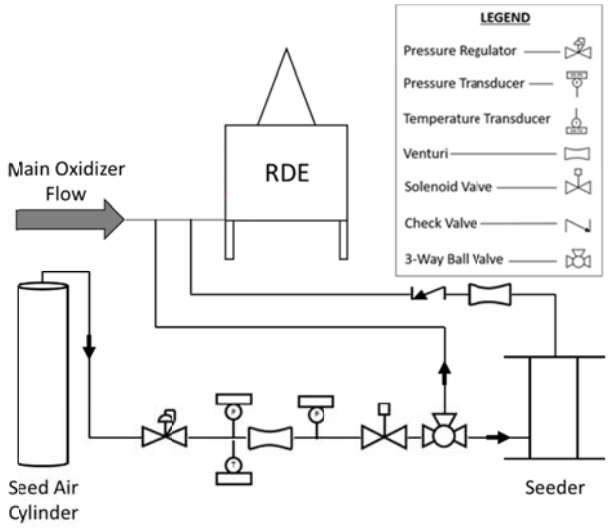

Figure 3a. P&ID DIAGRAM DETAILING INTEGRATION OF SEEDER TO FLOW SYSTEM.

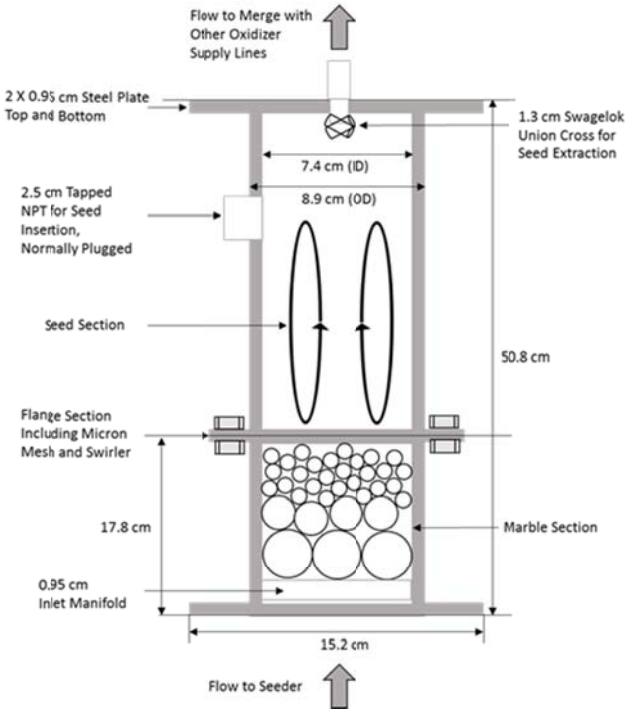

Figure 3b. SCHEMATIC DISPLAYING DETAILS OF SEEDER DESIGN FOR PIV DIAGNOSTICS.

The seed used for this study is 200 nm ZrO_2 nanoparticles. This seed was selected after careful consideration of potential safety hazards of introducing a metallic compound into a high pressure, oxygen-rich reacting environment. In another study, additional seed particles such as 20-30 nm SiO_2 and 40 nm TiO_2 were extensively investigated for PIV experiments in the exhaust flow of the RDC [35]. Unfortunately, these seed particles scattered insufficient quantity of light for valid PIV analysis because of the limitations of the laser hardware when operated at the requisite high pulse rates. Fortunately, continuous advancements in high-power pulsed lasers are expected to allow TR-PIV measurements with smaller seed

particles in future work than possible in the present study.

A Quantronix Hawk Duo 120 watt, 532 nm Nd-YAG laser is used for the TR-PIV system. Figure 4 displays a diagram of the sheet optics designed for this study to create the laser sheet. The laser beam passes first through a spherical lens with a focal length of 500 mm to optically focus the laser beam and thus, to maximize laser intensity, at the region of interest. The focal length of the spherical lens was selected based on laboratory spatial constraints. The beam then passes through two cylindrical lenses to generate the laser sheet; a concave lens with a focal length of -25 mm transforms the beam into a diverging laser sheet and a convex lens with a focal length of 75 mm is used to collimate the laser sheet. This optical arrangement resulted in a laser sheet with minimal divergence angle and a sheet height similar to that of the field of view of the camera, both important factors to maximize the light intensity of the laser sheet.

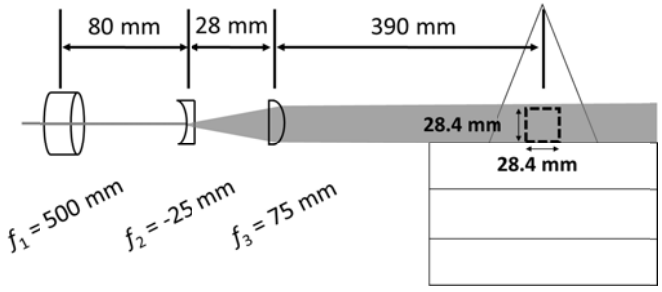

Figure 4. SCHEMATIC OF THE OPTICAL SYSTEM TO MAXIMIZE THE LASER SHEET INTENSITY.

The sheet thickness (0.97 peak intensity thickness) at the region of interest, measured by traversing a photodiode across the sheet, was approximately 1 mm. Thus, only seed particles flowing with normal velocity greater than 1000 m/s could cross the laser sheet during the 1 μs time between the laser pulses. Such high flow velocities normal to the laser sheet are not expected, an assumption partly supported by the measurements and previous literature [31]. The region of interest (or camera field of view) is a square sheet 28.4 mm x 28.4 mm along a cord of the annulus in the middle of the annular gap. The location of the measurement was radially centered in the annulus. The present PIV system measures only two velocity components in an otherwise 3D flow. It is assumed that the non-axial velocity component is purely circumferential, and it does not contain a radial component at the location of the region of interest. The flow field can therefore be discretized into axial and circumferential velocity components. Strictly, this assumption is valid only close to the centerline of the field of view, i.e., $x \cong 14.53$ mm where no net flow in the radial direction of the RDE is expected. However, it is acknowledged that away from the centerline of the field of view, contribution from the radial velocity component would be higher, and could affect the accuracy of the present circumferential velocity measurements.

A high-speed digital CMOS camera, Photron SA5 Fastcam, is used to acquire the PIV images at acquisition rate of 60 kHz. The camera is configured with a Sigma 105 mm focal length lens. A 532 nm band-pass optical filter was mounted in front of the camera lens to capture only the light scattered from the seed particles with the laser sheet. The camera is positioned perpendicular to the region of interest and 62 cm away from the laser sheet; the bottom edge of the laser sheet, i.e., $y = 0$ mm coincides with the exit plane of the back-pressure nozzle spool. An inspection window was cut into the protective Lexan blast shield enclosure to avoid distortion of PIV images by the intervening surfaces. Each PIV image was 320 x 320 pixels, which resulted in spatial resolution of 88.64 □m/pixel.

Figure 5 presents the PIV timing diagram to synchronize the laser pulses with the PIV image capture sequence. For PIV acquisition rate of 30 kHz, a pair of PIV images was acquired at every 33.3 μs. The time between the two consecutive laser pulses was set to 1.0 μs. This time was chosen after multiple trials to optimize the velocity resolution and image processing. The PIV timing sequence is implemented via a synchronizer controlled by the TSI Insight software. In addition, PIV image acquisition was initiated by the BeagleBone microprocessor system developed in-house to also control all other flow and diagnostic components. Given the cited spatial resolution and pulse width, the uncertainty in velocity measurements is ± 44.3 m/s.

Insight 4G Data Acquisition, Analysis, and Display software from TSI was used to process the PIV images to calculate the velocity components. Pixelated noise in the images was minimized using an image generator based on minimum intensity which was subtracted from the data set in an image calculator. Due to the high velocity of the RDE exhaust flow, a starting interrogation window of 96x96 pixels and final interrogation window of 48x48 pixels were used with a double

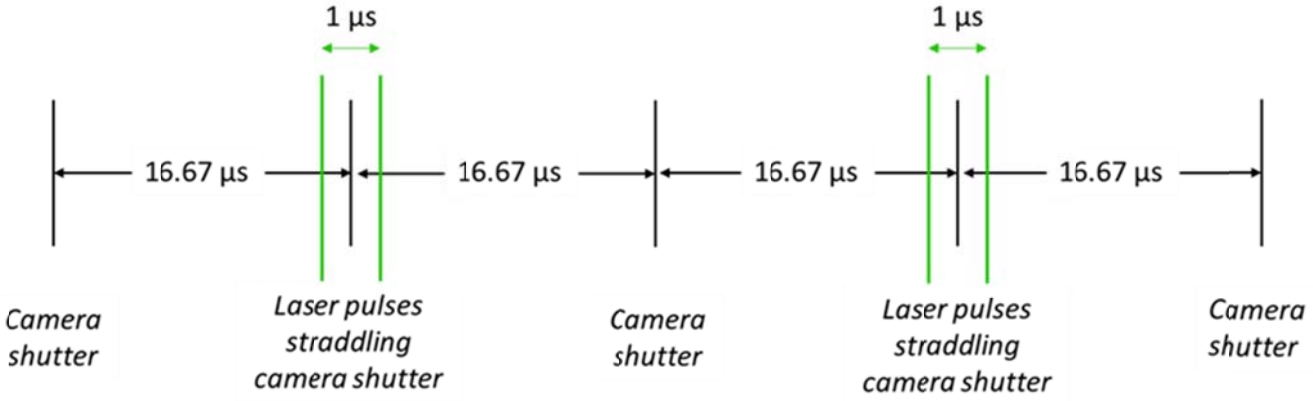

Figure 5. PIV TIMING DIAGRAM.

pass Recursive Nyquist grid. The correlation analysis of PIV data was performed with an FFTCorrelator, and the location of the correlation peak was determined by the Gaussian Peak technique which fits a Gaussian distributed curve fit to the highest pixel intensity and the four nearest neighboring interrogation cells. Computed velocity data was restricted to displacement of seed particles less than or equal to 30% of the starting spot interrogation window.

The resulting nodal-based velocity flow field data set was then post processed, first via a local validation method. This validation consisted of a universal median test, in which velocity measurements are compared to the local median of the 3x3 interrogation neighborhood of the specific node. Variations of twice the circumferential or axial velocity measurement from this local medium were discarded, and replaced by valid secondary peaks in the interrogation neighborhood when applicable. A conditioning process was also applied in the post processing of the data in which holes in individual vector flow field matrices were filled using the 3x3 local median. This recursive filling technique was applied using measured vectors in the interrogation neighborhood, and the process was omitted if only previously analytically replaced vectors were present.

RESULTS

Over 100 successful hot fire tests have been performed at UA, over two dozen of which to apply the PIV diagnostics and optimize its implementation. The results in this study will focus on an experiment in which the seed consistency and distribution was optimal, referred to as the primary experiment. Additionally, results from a secondary experiment conducted one week apart at the same flow conditions will be displayed to illustrate the repeatability of the PIV measurements. Multiple other tests performed over a period of three months revealed similar results, albeit with fewer valid data points. These other tests will not be shown separately considering that they matched with the data presented in this study. However, many of the significant and relevant details are available in a recent related publication [35].

The operating conditions for the test consisted of flow rates of 0.0467 kg/s for methane, 0.0894 kg/s for main air, 0.161 kg/s for O_2, and 0.0170 kg/s for seed air. These flow rates correspond to an equivalence ratio of φ=0.977, a heat release rate of 2.4 MW, and about 5.5% of the total mass flow rate going through the seeder. The operating conditions are similar to those considered in previous studies at UA, where detailed high-speed imaging and ion-probe data inside the RDE [33] and time-resolved OH* chemiluminesence imaging [34] at the RDE exit were presented. Figure 6(a) shows normalized pressure traces in reactant supply lines, and Fig. 6(b) shows the pressure within the RDC, as measured by the PC and CTAP static pressure probes. In the primary experiment, ion-probe measurements yielded an oscillation frequency of 6.1982 kHz, which corresponds to an average detonation wave speed of about 1,947 m/s inside the annulus. Both the primary and secondary experiments exhibited a single detonation wave mode, with the wave propagating in the clockwise direction when viewed from the RDE exit. The wave motion showed minor cycle to cycle variations at this test conditions as documented in detail in Ref 33.

In this section, TR-PIV results obtained at the exit of the RDE annulus configured with a back-pressure CD nozzle are presented. The test results for the primary experiment are based on 16,000 consecutive PIV image pairs corresponding to over half a second of flow field data. While the diagnostic technique and associated hardware will continue to be refined to quantify and reduce the measurement uncertainties, data repeatability will be demonstrated, and physical insights regarding the orientation, periodicity, and spatial and temporal variations of the shock laden flow field will be gained from the inspection of the results.

PIV Images and Velocity Vectors

Figure 7 shows a series of ten consecutive PIV images from the primary experiment to qualitatively assess the periodicity of the flow field. Each of these images pertains to the first of the PIV image pairs used for the analysis. The

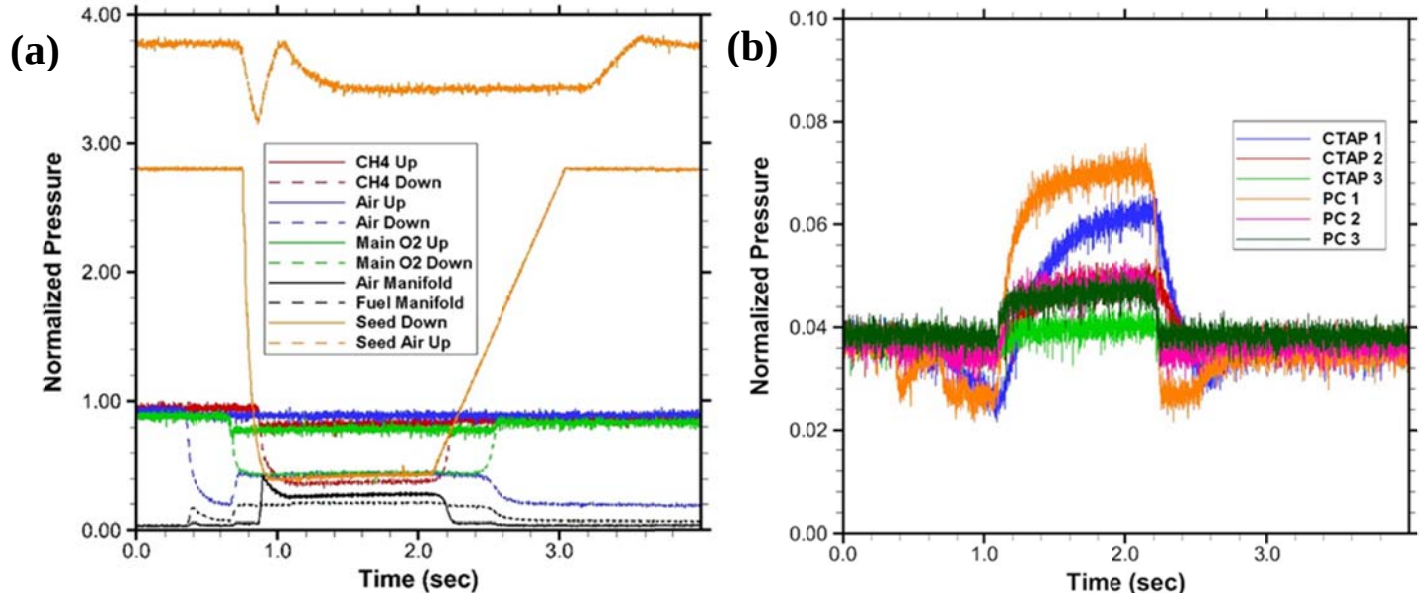

Figure 6. PRESSURE MEASUREMENTS IN (a) REACTANT LINES UPSTREAM OF THE RDC, AND (b) WITHIN THE RDC.

images represent two cycles of detonation, in a single wave mode, given the 30 kHz PIV acquisition rate and wave rotation frequency of about 6,200 Hz as measured by the several high-frequency ion-probe sensors placed on the RDE spools. The detonation wave and the oblique shock wave propagate inside the RDE in clockwise direction (right to left) as confirmed by the ion-probe sensors and two high-speed cameras. In the first image of each row, the bright region represents the oblique shock wave passing through the field of view. The high velocity regions of the shock entrain the seed, and possibly agglomerate it, to brightly illuminate the shock structures compared to other regions of this high temperature flow of combustion products. Much less brightness is observed in the next two images, suggesting sparsely distributed seed particles, and hence, small flow velocities at these instants. The bright regions increase in the next two images, and the cycle repeats itself as shown by the consecutive images in the second row. This cyclic nature of the PIV images was consistent at all times of PIV acquisition

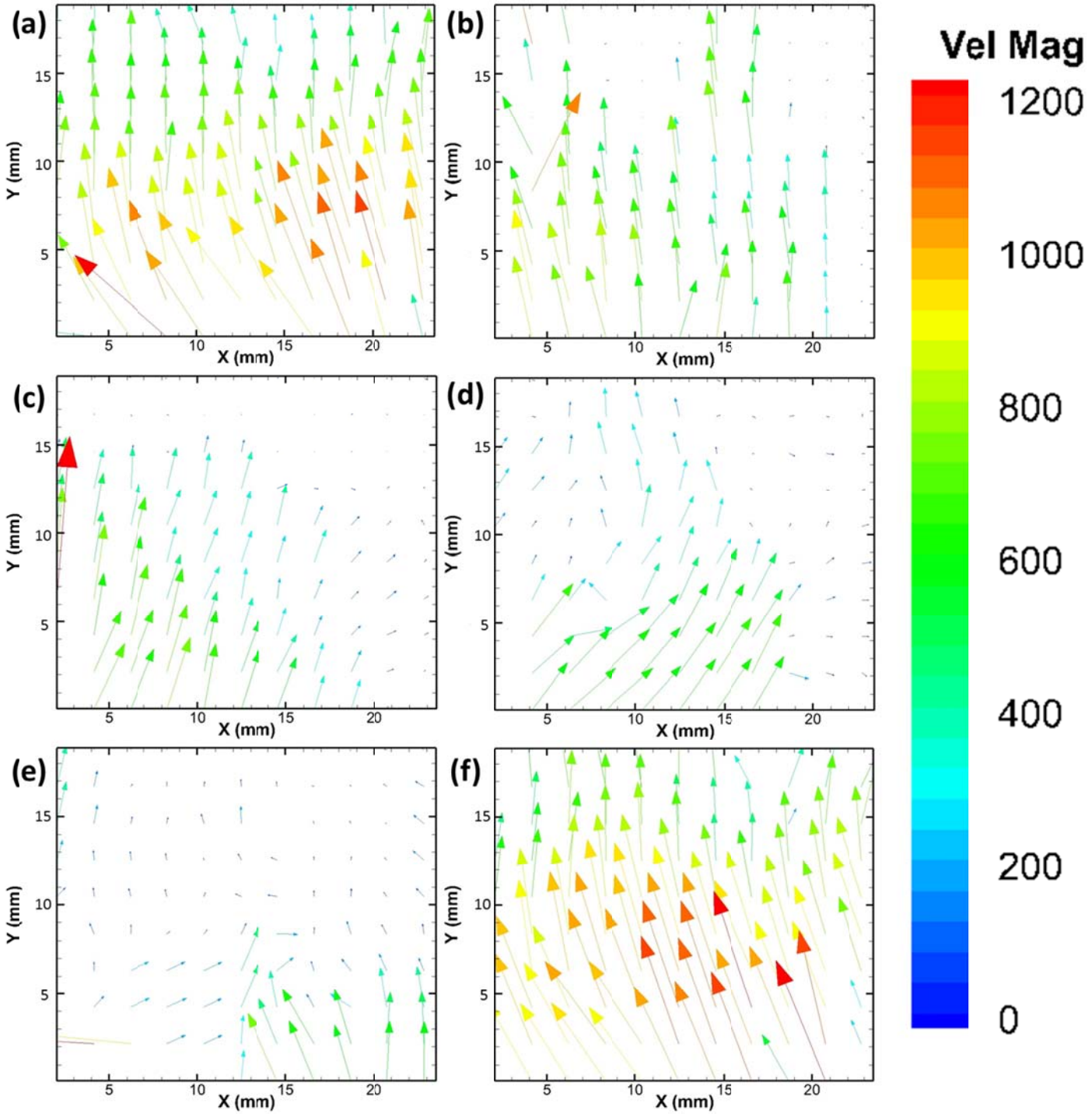

Figure 8. INSTANTANEOUS FLOW FIELD AT THE RDE EXIT DURING A PERIODIC CYCLE. RDE EXIT PLANE IS AT Y = 0 MM, AND X = 14. 53 MM IS LOCATION NEAR CENTERLINE INTERSECTING WITH RDE RADIUS. THE TIME INTERVALS BETWEEN PLOTS IS 33.3 MICROSECONDS.

during the RDE operation, and in tests acquired over a period of three months.

Figure 8 displays the velocity vectors for the first six PIV images shown in Fig. 7 to illustrate the quantitative details of the time dependent period flow field. The first plot, Fig. 8(a), shows that although the flow is primarily axial at downstream locations (y > 5 mm), it is oriented right to left indicating a significant circumferential velocity component at the RDE exit (y < 5 mm) coinciding with the direction of the clockwise wave rotation within the combustor annulus. Maximum velocities are observed immediately behind the shock front in the expansion regime. The second plot, Fig. 8(b), shows a predominantly axial flow field immediately after the oblique shock wave front has exited the PIV field of view. The third and fourth plots in Fig. 8 shows that the flow has tilted towards the right side, i.e., circumferential velocity component direction is opposite to that of the wave rotation, as combustion products move away from wave front.

In the fifth plot, the flow velocities are relatively small, indicating conditions imminent to the arrival of the next wave front. At this instant, the flow direction is inconsistent, and localized eddies counter to the direction of wave propagation are also observed. In the next plot, high velocity flow field tilted towards the left reappears to indicate the arrival of the next wave front to repeat the cycle. The first and the last plots in Fig. 8 are similar, though not identical, since the fixed acquisition rate of 30 kHz does not exactly match the cycle period. The cycle repeats between 5th and 6th plots indicating that the cycle time (period) is between 133.2 and 166.5 □s. These results show clearly that the RDE exit flow is highly periodic with an oscillation frequency between 6,000 and 7,500 Hz. Significant flow oscillations occur both in axial and circumferential directions. Moreover, the circumferential flow changes direction across the wave front, in the same direction ahead of the wave front and the opposite of it behind the wave front, an observation in agreement with numerical simulations of Nordeen et al [31].

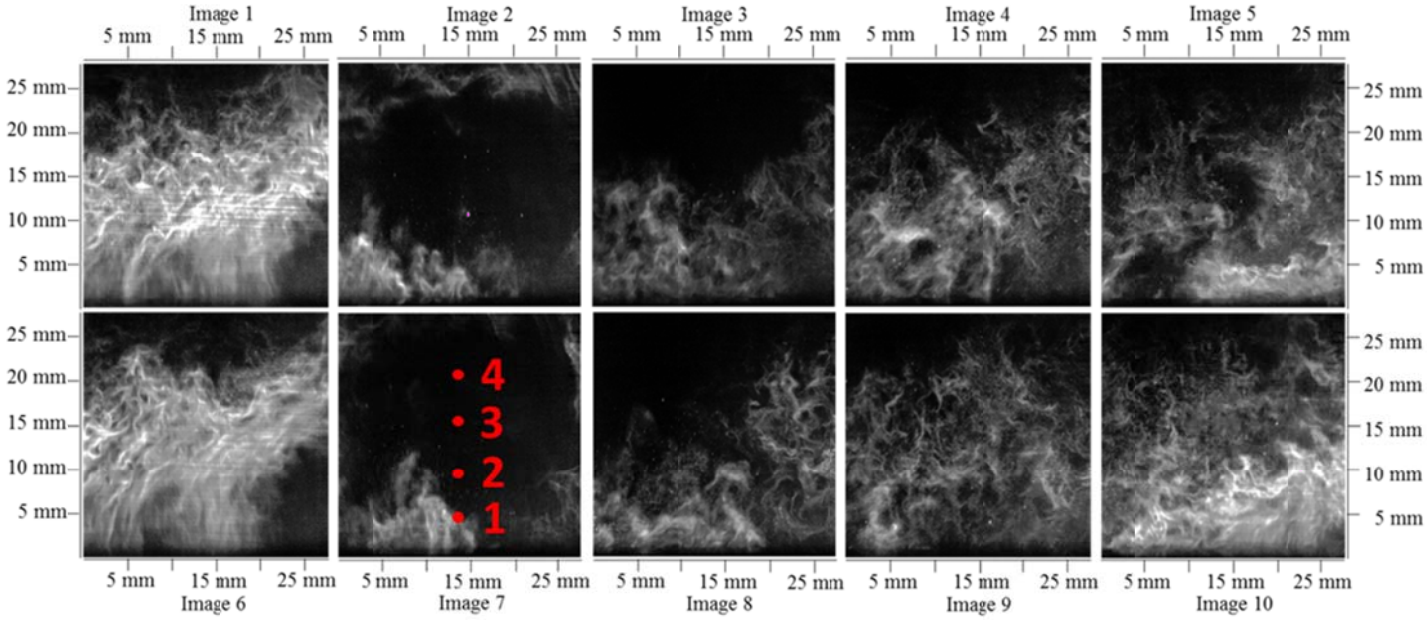

Figure 7. A SAMPLE OF PIV IMAGES ACQUIRED IN THE EXPERIMENT. ONLY THE FIRST OF EACH IMAGE PAIR IS SHOWN. IMAGES ARE AT 33.3 μs INTERVAL, FROM LEFT TO RIGHT, AND TOP TO BOTTOM.

Analysis of PIV Results

Four discrete nodal points within the PIV region of interest were inspected to quantitatively assess the large amount of the PIV data acquired. These points, identified by red dots in a frame of Fig. 7, were all selected from the most centered of the vector nodes after processing the PIV images, i.e. at x = 14.53 mm, and y = 4.9 mm, 9.0 mm, 15.2 mm, and 21.5 mm, where y = 0.0 mm represents the exit plane of the RDE. The same nodal locations were used for analysis in the primary and secondary experiments. As discussed previously, the assumption of a 2D flow field discretized into axial and circumferential components is most valid at these points. In this section and throughout this study, positive circumferential velocity values will correspond to flow in the counter-clockwise direction (CCW) or left to right, while negative circumferential velocity values correspond to flow in the clockwise (CW) direction or right to left.

Figure 9 presents an overview of the results from the PIV analysis at point 1, i.e., x = 14.53 mm and y = 4.9 mm for the primary experiment. Figure 9(a)-(b) show the axial and circumferential velocity measurements for the entirety of the PIV acquisition, while Fig. 9(c)-(d) show only 0.1 sec of test results to better distinguish individual data points. These so-called scatter plots show that the axial velocity varies throughout the test, with the majority of measurements between 0 and 1250 m/s while some outliers with values up to 2000 m/s are also observed. The velocity values at either extreme are subject to greater uncertainties, partially attributed to insufficient seed and/or imperfect seed distribution.

As previously observed in Fig. 8, the circumferential velocity measurements are shown to have both positive and negative values. The majority of these measurements range between -350 m/s to 400 m/s, though outliers outside these bounds are also observed. Results clearly demonstrate that the flow field fluctuates in both axial and circumferential directions. Moreover, these results provide indisputable

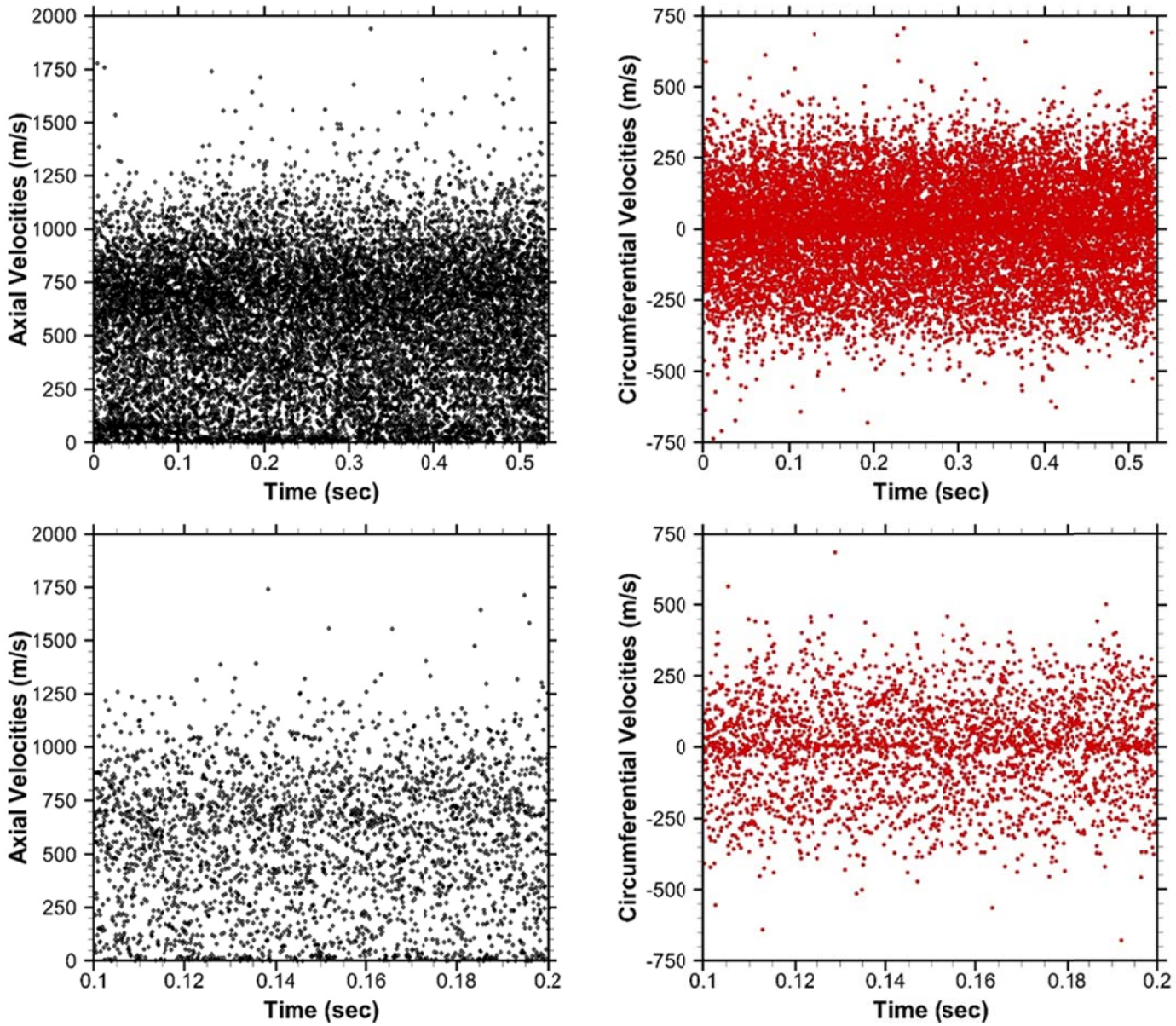

Figure 9. OVERVIEW OF PIV RESULTS FOR PRIMARY TEST CASE FOR THE ENTIRE TEST DURATION (a&b) AND FOR 0.1 S SEGMENT (c&d). AXIAL VELOCITIES ON LEFT (a&c), CIRCUMFERENTIAL VELOCITIES ON RIGHT (b,d).

evidence of significant circumferential velocity fluctuations at the RDE exit, an observation not yet quantified in experimental literature, though documented in computational studies [31-32].

While the measurements displayed in Fig. 9 correspond to the primary experiment, they agreed the secondary experiment, as well as other PIV data acquired at this flow condition. Another study conducted by the research group at UA using a different laser system presents results from additional tests, one conducted at the present flow condition and another at a higher flow rate of reactants [35]. That study shows similar quantitative results proving reliably of the present PIV diagnostics.

Figure 10 presents measurements at various points organized into histogram plots. Here, the primary and secondary experiments are compared to observe the similarities in the distribution of velocity measurement values. For all three points inspected in Fig. 10, both experiments showed strong agreement with each other, again indicating that the PIV data are repeatable. For point 1 in the primary experiment, the histogram in Fig. 10(a) reveals that the most densely populated axial velocity range is between 657 and 766 m/s, comprising 15% of all data points. Over 60% of the axial velocity measurements are between 329 m/s and 875 m/s, and nearly 2/3rd of the data points exceed 438 m/s. Meanwhile, Fig. 10(a) reveals an asymmetric distribution of axial velocity with minimum threshold of about 0 m/s.

Several interesting observations are made from the histogram of the circumferential velocity at point 1 in Fig. 10(b) for the primary experiment. Nearly 17% of measurements from the primary experiment are between -26.8 m/s and 54.6 m/s, when the flow is primarily axial. However, 44% of the measurements have circumferential velocity greater than 54.6 m/s (CW), and about 40% of data indicate negative circumferential velocity of less than -26.8 m/s (CCW). The data distribution suggests that near the RDE exit at point 1, the flow oscillates axially and circumferentially in and counter to the direction of rotation for the detonation and oblique shock waves within the RDE annulus.

Figure 10(c)-(d) show respectively the histograms of axial and circumferential velocity measurements at point 2, i.e., x = 14.53 mm and y = 9.0 mm. At this downstream location, the overall trends agree with those upstream at point 1. The asymmetric nature of the axial velocity histogram is similar to that at point 1. However, 10.7% of axial velocity measurements of the primary experiment at point 2 are between -37.8 m/s and 30.9 m/s. At point 2, the circumferential velocity component is more densely distributed at the mean value of about 0 m/s. Figure 10(e)-(f) show that the axial velocity histogram at point 3 is similar to those at points 1 and 2 for values greater than 200 m/s. Likewise, the asymmetric distribution of the axial velocity at the downstream location is similar to that at the two upstream points.

Increasing occurrence of low axial velocity regions at downstream locations can be attributed to multiple reasons. One cause could be the existence of localized flow recirculation regions with vortical structures caused by the rarefaction events following shock events. Second, portions of the PIV measurements might be compromised by insufficient seed in these low velocity regions, yielding greater inaccuracies in the PIV analysis. Lower circumferential velocity at the downstream location indicates diminishing rotation as the flow expands into the ambient.

Analysis of Flow Periodicity

Next, measurements were scrutinized for a brief test duration of 1 ms, representing about six oscillations cycles, to discern the relationship between the two velocity components. Figure 11 presents these measurements for the four selected points. Measurements from both the primary and secondary experiments are shown for comparison. The points correlated to test segment about 0.217 sec after ignition for the primary experiment and 0.312 sec after ignition for the secondary experiment. Note that although the data points in the plots are connected by lines for aide in visualization, these points separated by 33.3 μs time interval are sequential measurements, and should not be interpreted as perfectly replicating the periodic flow field. Yet, interesting trends of flow periodicity can be observed; the axial velocity undergoes a steep velocity increase within each cycle, and at the same time, the circumferential velocity reaches a local minimum indicating a clockwise flow orientation. Maximum velocity magnitudes are observed both along the finite oblique shock front, as well as in the expansion region immediately following it. These instances are represented by images 1 and 6 in Fig. 7, and frames (a) and (f) in Fig. 8. While maximum CW oriented circumferential velocities are associated with measurements acquired at the oblique shock front, those in the expansion regime have low circumferential velocities, indicating primarily axial flow. This non-axial component of the flow then trends positive (CCW), indicating "tilt" of the flow in the direction opposite to the detonation wave propagation as the axial velocity decreases. Immediately preceding the arrival of the next shock wave, both the axial and circumferential velocity components are observed at the lowest values. Upon arrival of the shock front, the axial velocity increases, and the circumferential velocity again "tilts" in the direction of the propagating shock (CW).

These results further confirm observations made from the interpretation of PIV images: the flow field is highly period and heavily influenced by the oblique shock wave passing the field of view at all four selected nodal locations. These trends are consistent in both the primary and secondary experiments. Note deviations in velocity peaks are caused by minor differences in the acquisition time for the two case, and the rapid changes in flow velocity occurring during the period cycle. Results demonstrate the switching of the flow orientation and are consistent with computational studies to characterize the circumferential flow field at the RDC exit [32].

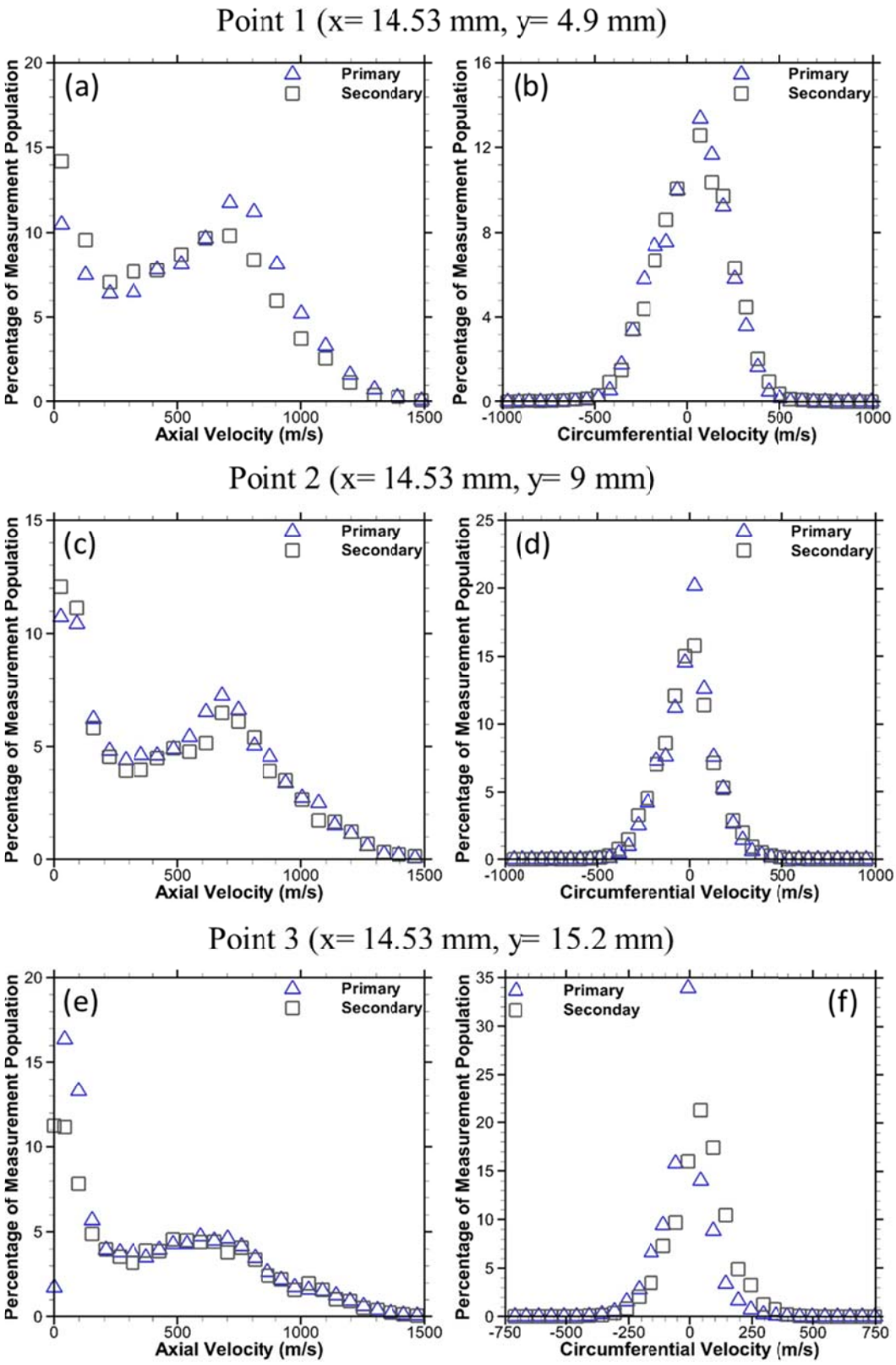

Figure 10. HISTOGRAMS OF AXIAL AND CIRCUM. VELOCITIES AT PT. 1 (a&b), PT. 2 (c&d), AND PT. 3 (e&f) FOR BOTH THE PRIMARY AND SECONDARY EXPERIMENTS.

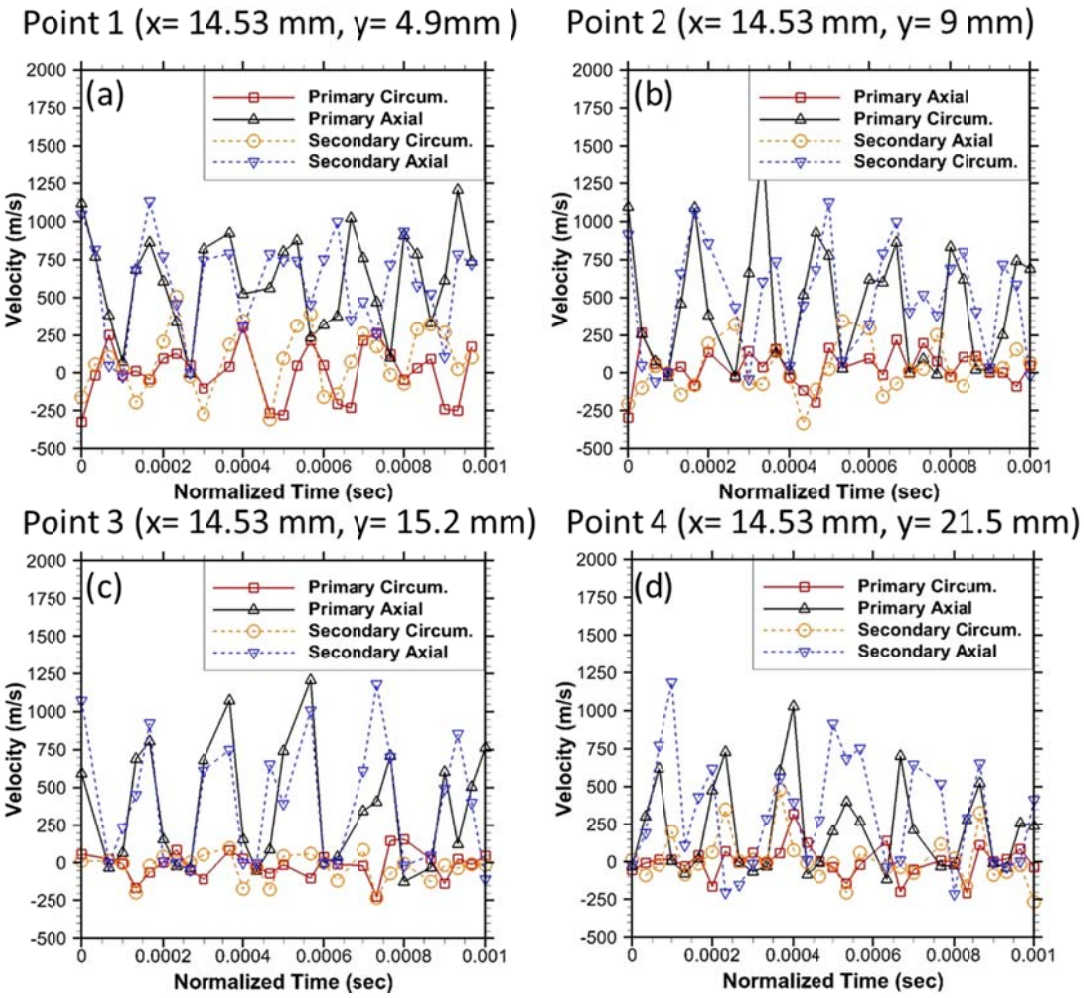

Figure 11. AXIAL AND CIRCUMFERENTIAL VELOCITY MEASUREMENTS FOR BOTH PRIMARY AND SECONDARY EXPERIMENTS DURING 0.001 SEC FOR PT. 1 (a), PT. 2, (b), PT. 3 (c), AND PT. 4(d).

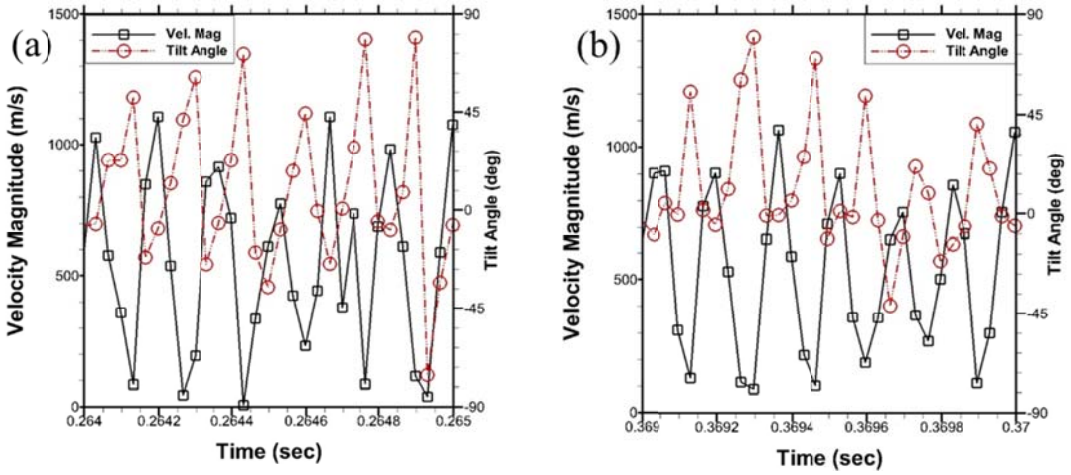

Figure 12. PLOTS OF VELOCITY MAGNITUDE VS. FLOW TILT ANGLE FOR TWO 0.001 SEC TIME SEGMENTS FOR PRIMARY EXPERIMENT.

Next, the tilt angle of the flow is more closely inspected. The positive angle is associated with CCW flow orientation and vice versa. Figure 12 present the flow "tilt" angle as it relates to the total velocity magnitude at point 1 for two different time segments of the primary test case. Trends observed in earlier plots are again evident in these plots. The flow tilt angle reaches local maxima (CCW) as the velocity magnitude reaches

local minima. This portion of the cycle is associated with regimes immediately preceding the passing of the shock wave through the relative PIV view frame. These events are followed by a sharp increase in velocity magnitude as the shock wave propagates across the PIV interrogation window.

Phase Resolved Cycle Reconstruction

Previous plots provide useful insights into the periodic nature of the flow field, but TR-PIV at 30 kHz is still inadequate to fully describe the periodic flow field on an instantaneous basis. Thus, it is desired to construct a phase-resolved cycle using PIV data from multiple cycles during the

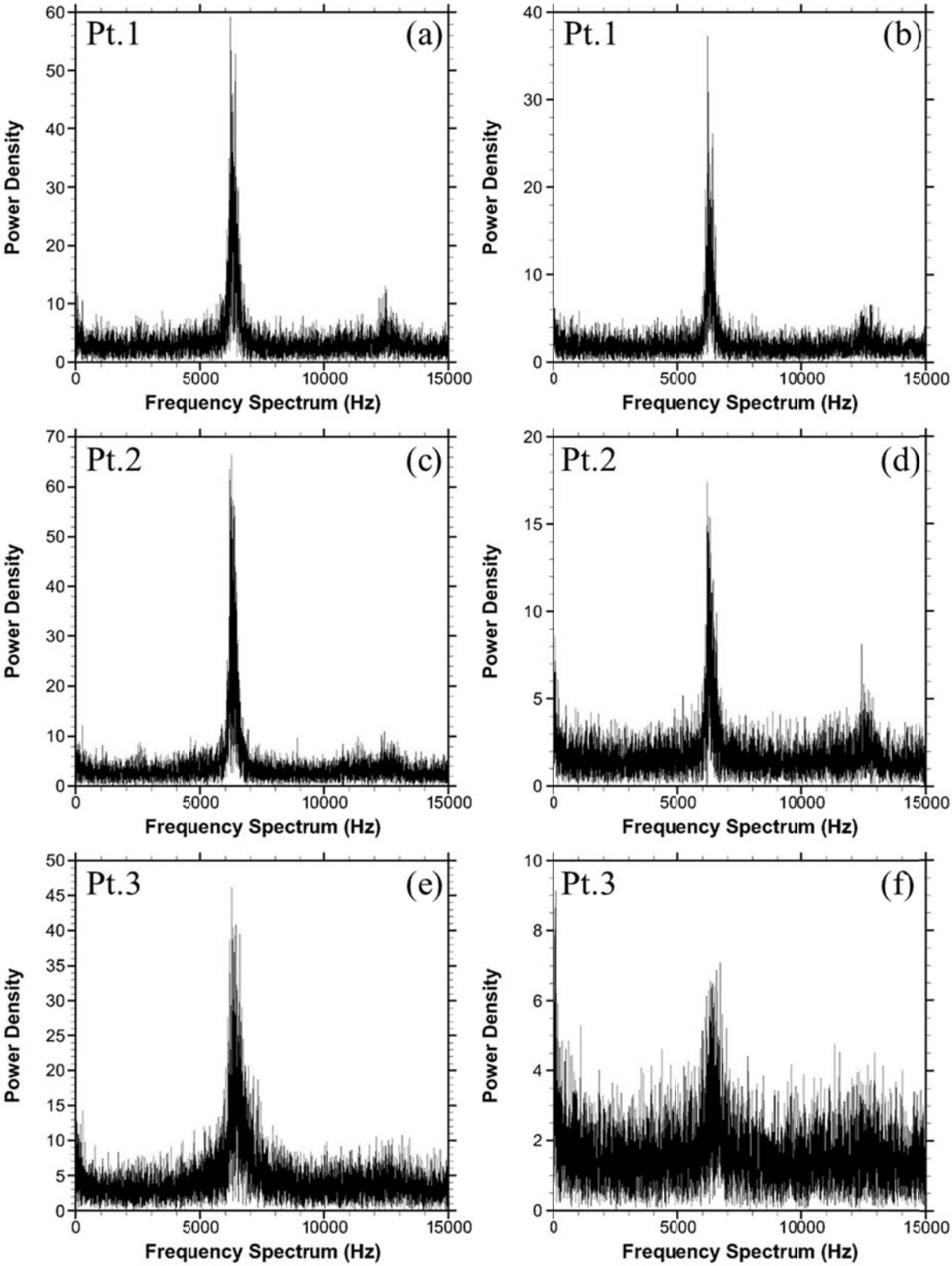

Figure 13. POWER DENSITY SPECTRA OF AXIAL (a,c,e) AND CIRCUMFERENTIAL (b,d,f) VELOCITY MEASUREMENTS FOR PRIMARY EXPERIMENT AT: POINTS 1 (a&b), 2 (c&d), AND 3 (e&f).

test. In the absence of an exact reference time to identify the start and end of each cycle in the field of view, the PIV data were processed to determine the dominant oscillation frequency using fast Fourier transform (FFT) analysis of axial and circumferential velocity data.

Figure 13 displays the resulting frequency spectrum for the axial (a, c, e) and circumferential (b, d, f) velocity components for points 1 (a and b), point 2 (c and d), and point 3 (e and f). Both the axial and circumferential velocity spectra at point 1 yield a peak power density at a frequency of 6,210 Hz, but both also exhibit a secondary peak at a frequency of 6,405 Hz. These two peaks are close to the peak frequency of 6,198 Hz measured by the ion-probes. Similar results are obtained at downstream locations, where the power density becomes more distributed across the peak frequencies. This distribution of power density across multiple peaks is attributed to variations in the periodicity of RDC operation. While the primary mechanism contributing to this incongruity has not yet been identified, the cycle-to-cycle variation in the wave speed has been documented previously [33, 34], and it makes it difficult to perform the phase-resolved cycle reconstruction analysis. Thus, a spectrogram based on velocity measurements was generated to inspect the cycle-to-cycle variations in the flow frequency, and to identify time intervals with the least variations. Figure 14 (a) shows the spectrograms for the circumferential velocity data at point 1 and Fig. 14 (b) shows the spectrograph for pressure data acquired at a high sampling rate (1 MHz) by a PCB dynamic transducer recess mounted at the RDC annulus outer wall in the second spool. The frequency axis is zoomed around regions of peak power density between 5.5 kHz and 7.0 kHz. Though the oscillation frequency varies during the test, small segments with relatively constant frequency are also observed. The time segment with the least variation in cycle-to-cycle frequency was identified by calculating the minimum frequency gradient (with time) in the

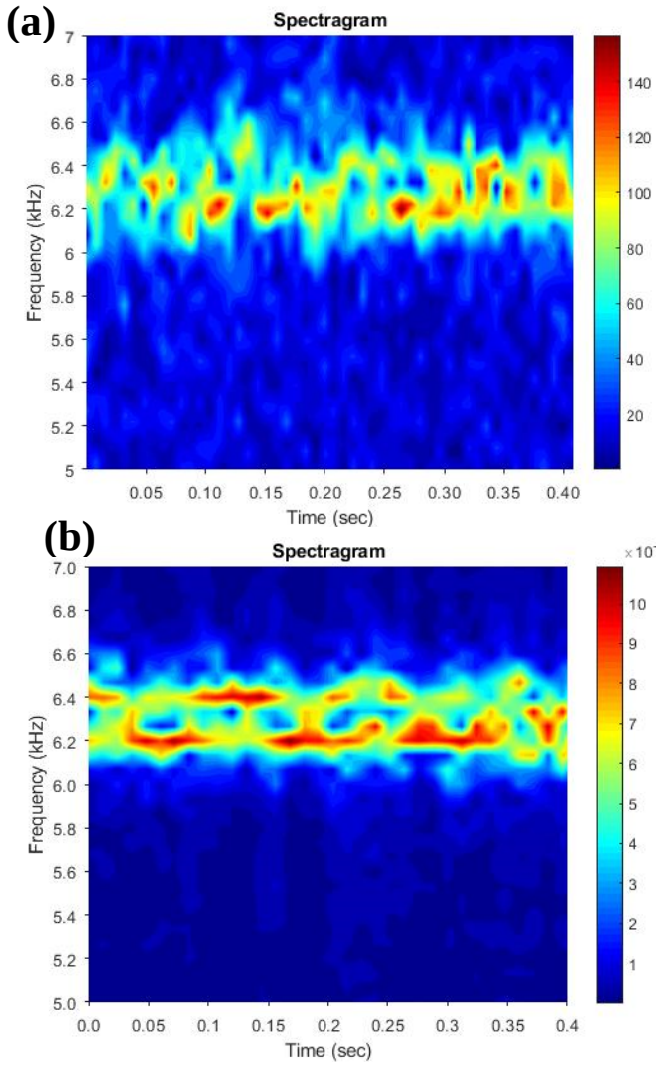

Figure 14. SPECTROGRAM OF (a) CIRCUMFERENTIAL VELOCITY DATA AT POINT 1, AND (b) HIGH FREQUENCY PRESSURE DATA ACQUIRED BY PCB PROBE, RECESS MOUNTED TO RDC ANNULUS OUTER WALL.

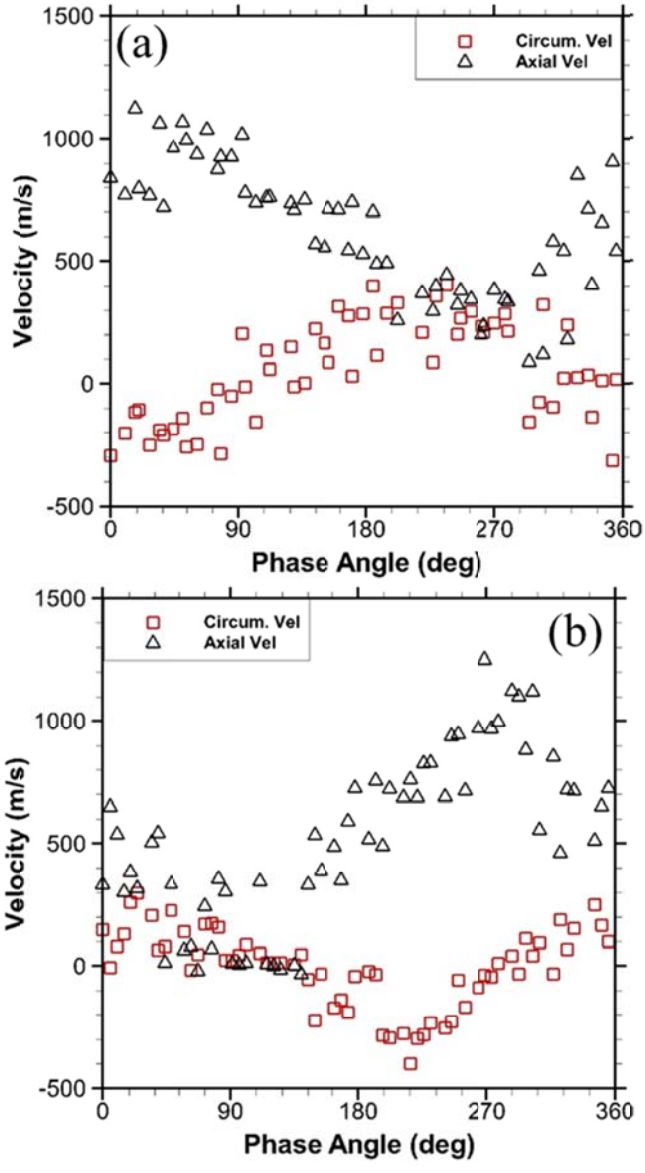

Figure 15. RECONSTRUCTED PHASE-AVERAGED CYCLES USING DATA FROM TWO TIME SEGMENTS: (a) 0.1883-.1904 SEC, and (b) 0.2167-0.2187 SEC.

spectrogram.

The corresponding data was used to reconstruct the phase-averaged cycle presented in Figure 15 for two different time segments. The dominant frequencies used to reconstruct Fig. 15(a)-(b) were 6,400 Hz and 6,421 Hz, respectively. Though the cycles do not align perfectly because of the arbitrary phase angle assignment, the overall trends and magnitudes of axial and circumferential velocity are similar in both time segments. The scatter in the plots is attributed to still unresolved cycle-to-cycle variations, and to fluctuations inherently present in a turbulent flow. The axial velocity measurements show a steep positive slope as the oblique shock wave crosses the field of view and the velocity values rise quickly. At this time, the circumferential velocity has negative values corresponding to the clockwise orientation of the detonation wave propagation. In the expansion regime following the passing of the shock wave, the axial velocity maximum is reached. In this regime, low circumferential velocity values indicate that the flow is primarily axial. Then, the circumferential velocity undergoes "tilt" in a direction opposite to that of the detonation wave while axial velocity reaches a minimum. More precise phase-resolved velocity measurements are expected at high reactant flow rates, when the cycle-to-cycle variations are significantly smaller as demonstrated by Welch et al. [33], but Fig. 15 helps establish the phase relationship between the two velocity components.

CONCLUSIONS

In this study, time-resolved particle image velocimetry at an image pair acquisition rate of 30 kHz was used to characterize the flow field, oscillating at a frequency of greater than 6 kHz, immediately at the exit a rotating detonation engine operating with methane fuel and oxygen enriched oxidizer and configured with a back-pressure plate to simulate power generating gas turbines. For the primary experiment, the diagnostic was successful in acquiring over 16,000 consecutive PIV image pairs, corresponding to over 0.53 sec of test data. Measurements were acquired on a 2D plane along the cord length where the PIV data could be approximately discretized into axial and circumferential velocity components. Analysis of the PIV data resulted in the following conclusions:

- Inspection of PIV images led to the observation of an oblique shock structure propagating in the same direction as the detonation wave and oblique shock wave inside the annulus. The vectors plots indicated that the instantaneous flow field varied significantly with time in a periodic manner.
- The histograms at four nodal points along the flow direction revealed an asymmetric distribution for the axial velocity and a nearly symmetric distribution for the circumferential velocity with mean value for the latter of about 0 m/s.
- The phase relationship between velocity oscillations revealed that an increase in the axial velocity coincided with the passing of oblique shock structure. Behind the oblique shock structure, the axial flow velocity decreased as the flow in the circumferential direction reversed away from the oblique shock structure. The circumferential velocity in the counter clockwise orientation was largest when the axial velocity was minimum. These results are consistent with computational studies of RDC exhaust flow field, such as those conducted by Nordeen et al. [32].
- The primary experiment was compared with a secondary experiment conducted at the same operational conditions. The results of the two experiments yielded similar quantitative trends in the oscillatory flow behavior indicating that the PIV data are repeatable.
- FFT analysis was performed to reveal that the flow field oscillated at nearly the same frequency as the detonation wave and oblique shock wave within the RDE, proving direct evidence that the detonation wave motion indeed affects the downstream flow field.
- Spectrogram from velocity measurements was utilized to isolate test segments with minimum cycle-to-cycle variations and thus, to reconstruct the phase-resolved axial and circumferential velocity profiles for an oscillation cycle. Results show trends observed in other plots, but also indicate that cycle-to-cycle variations can be difficult to account for accurately.

Several improvements to the PIV diagnostic can be made for future studies. For example, experimental uncertainties related to spatial and temporal non-uniformities in seed distribution must be quantified and minimized, although this is a difficult task to realize in practice because of the high temperature, and large temporal and spatial variations in the flow velocities. Temporal incongruities in seed distribution can contribute to portions of the flow being unresolved, which affects the validation of neighboring cells. Additionally, smaller seed particles should be used to reduce the relaxation time [40-41], but it will require pulse lasers with higher power. Additionally, the effect of laser light intensity, time between laser pulses, laser sheet thickness, laser pulse duration, and laser frequency are important issues, and should be addressed in future studies. For example, it was determined that while the intensities delivered from two separate laser diode heads for pulse "A" and pulse "B" could be manipulated to an extent, there were still disparities in intensity between the two laser sheet. These disparities should be minimized further to the extent possible within the hardware limitations in future studies.

While this study confirmed that TR-PIV is feasible in the periodic, supersonic, high temperature environment immediately outside the RDE, future studies should aim to acquire flow measurements within the RDE at multiple operating conditions, without and with flow conditioning de vices integrated into the RDE hardware, to not only quantify the pressure gain but also to minimize the overall pressure loss while meeting the flow requirements at the turbine inlet.

ACKNOWLEDGEMENTS

This material is based upon work supported by the Department of Energy under Award Number(s) DE-FE0023983.

Disclaimer: "This report was prepared as an account of work sponsored by an agency of the United States Government. Neither the United States Government nor any agency thereof, nor any of their employees, makes any warranty, express or

implied, or assumes any legal liability or responsibility for the accuracy, completeness, or usefulness of any information, apparatus, product, or process disclosed, or represents that its use would not infringe privately owned rights. Reference herein to any specific commercial product, process, or service by trade name, trademark, manufacturer, or otherwise does not necessarily constitute or imply its endorsement, recommendation, or favoring by the United States Government or any agency thereof. The views and opinions of authors expressed herein do not necessarily state or reflect those of the United States Government or any agency thereof."

REFERENCES

[1] Zel'dovich, Y.B. "Energy utilization of detonation combustion." *Zh. Tekh. Fiz*., Vol. 10, No. 17, (1940): pp. 1455-1461.

[2] Frolov, S.M., Aksenova, V., Guseva, P.A., Ivanova, V., Medvedeva,, S.N., and Shamshina, I. "Experimental Proof of the Energy Efficiency of the Zel'dovich Thermodynamic Cycle." *Physical Chemistry* Vol. 459 Part 2 (2014): pp. 207-211.

[3] Frolov, S.M., Aksenova, V., Ivanova, V. "Experimental proof of Zel'dovich cycle efficiency gain over cycle with constant pressure combustion for hydrogen-oxygen fuel mixture." *International Journal of Hydrogen Energy* Vol. 40 (2015): pp. 6970-6975.

[4] Sousa, J., Paniagua, G., and Morata, E.C. "Thermodynamic analysis of a gas turbine engine with a rotating detonation combustor." *Applied Energy* Vol. 195 (2017): pp. 247-256.

[5] Kailasanath, K. "Recent developments in the research on pulse detonation engines." *AIAA Journal* Vol. 41 No. 2 (2003): pp. 145-149.

[6] Roy, G.D., Frolov, S.M., Borisov, A.A., and Netzer, D.W. "Pulse detonation Propulsion: Challenges, Current Status, and Future Perspective." *Progress in Energy and Combustion Science* Vol. 30, No. 6 (2004): pp. 545-672.

[7] Voitsekhovskii, B.V. "Stationary spin detonation." *Sov. J. of Applied Mechanics and Technical Physics* No. 3 (1960) pp. 157-164.

[8] Nicholls, J.A., and Cullen, R.E. "The Feasibility of a Rotating Detonation Wave Rocket Motor." Univ. of Michigan, TR-RPL-TDR- 64-113, Ann Arbor, MI, 1964.

[9] Nakagami, S., Matsuoka, K., Kasahara, J., Kumazawa, Y., Fujii, J., Matsuo, A., and Funaki, I. "Experimental Visualization of the Structure of Rotating Detonation Waves in a Disk-Shaped Combustor." *Journal of Propulsion and Power* Vol. 33, No. 1, (2017).

[10] Stoddard, W.A., St. George, A, Driscoll, R., Anand, R., and Gutmark, E.J. "Experimental Validation of Expanded Centerbodiless RDE Design." *54th AIAA Aerospace Sciences Meeting*. 2016-0128, San Diego, California January 4-8, 2016.

[11] Wei, L., Jin, Z., Shijie, L., and Zhiyong, L. "An experimental study on CH4/O2 continuously rotating detonation wave in a hollow combustion chamber." *Experimental Thermal and Fluid Science* Vol 62 (2016): pp 122-130.

[12] Roy, A., Ferguson, D., Sidwell, T., O'Meara, B., Strakey, Peter, B., Clinton, and Sisler, A. "Experimental Study of Rotating Detonation Combustor Performance under Preheat and Back Pressure Operation." *55th AIAA Aerospace Sciences Meeting*. AIAA 2017-1065, Grapevine, Texas, January 9-13, 2017.

[13] Pandiya, N., St. George, A., Driscoll, R., Anand, V., Malla, B., Gutmark, E.J. "Efficacy of Acoustics in Determining the Operating Mode of a Rotating Detonation Engine." *54th AIAA Aerospace Sciences Meeting*. AIAA 2016-1649, San Diego, California, January 4-8, 2017.

[14] Lu, F.K. and Braun, E.M., "Rotating Detonation Wave Propulsion: Experimental Challenges, Modeling, and Engine Concepts." *Journal of Propulsion and Power* Vol. 30, No. 5 (2014) p. 1125-1142.

[15] Wolanski, P. "Detonative Propulsion." *Proceedings of the Combustion Institute*, Vol. 34, Issue 1 (2013): pp. 125-158.

[16] Bykovski, F.A. and Zhdan, S.A. "Current Status of Research of Continuous Detonation in Fuel–Air Mixtures (Review)." *Combustion, Explosion and Shock Waves*, Vol. 51, no.1 (2015) pp.21-35.

[17] Kailasanath, K. "Recent Developments in the Research on Rotating-Detonation-Wave Engines." *55th AIAA Aerospace Sciences Meeting*, AIAA 2017-07849-13, Grapevine, Texas, January 9-12, 2017.

[18] Rankin, B.A., Fotia, M.L., Naples, A.G., Stevens, C.A., Hoke, J.L., Kaemming, T.A., Theuerkauf, S.W., and Schauer, F.R. "Overview of Performance, Application, and Analysis of Rotating Detonation Engine Technologies." *Journal of Propulsion and Power* Vol. 33, Special Section on Pressure Gain Combustion (2017): pp. 131-143.

[19] Dyer, R., Naples, A., Kaemming, T., Hoke, J., and Schauer, F. "Parametric Testing of a Unique Rotating Detonation Engine Design." *50th AIAA Aerospace Sciences Meeting including the New Horizons Forum and Aerospace Exposition*. AIAA 2012-0121, Nashville, Tennessee, January 9-12, 2012

[20] Shank, J.C., King, Paul I., Karnesky, J., Schauer, F., and Hoke, J.L. "Development and Testing of a Modular Rotating Detonation Engine." *50th AIAA Aerospace Sciences Meeting including the New Horizons Forum and Aerospace Exposition*. AIAA 2012-0120, Nashville, Tennessee, Januray 09-12, 2012.

[21] Naples, A., Hoke, J., Karnesky, J., and Schauer, F. "Flowfield Characterization of a RDE." *51th AIAA Aerospace Sciences Meeting including the New Horizons Forum and Aerospace Exposition*. AIAA Paper No. 2013-0278, January 7-10, 2013.

[22] Fotia M.L., Hoke, J.L., and Schauer, F. "Propellant Plenum Dynamics in a Two-dimensional Rotating Detonation Experiment." *52nd AIAA Aerospace Sciences Meeting*. AIAA Paper No. 2014-1013, National Harbor, Maryland, January 13-17, 2014.

[23] Rankin, B., Hoke, J., and Schauer, F. "Periodic Exhaust Flow through a Converging-Diverging Nozzle Down-stream of a RDE." *52nd AIAA Aerospace Sciences Meeting.* AIAA 6.2014-1015, National Harbor, Maryland, January 13-17, 2014.

[24] Fotia M.L., Schauer F., Kaemming T., and Hoke, J. "Study of the Experimental Performance of a Rotating Detonation Engine with Nozzled Exhaust Flow." *53rd AIAA SciTech Forum*. AIAA 6.2015-0631. Kissimmee, Florida, January 5-9, 2015.

[25] Rankin B.A., Richardson, D. R., Caswell A.W., Naples A.G., Hoke J.L., Schauer F.R. "Chemiluminescence imaging of an optically accessible non-premixed rotating detonation engine." *Combustion and Flame* Vol. 176. (2016) 12-22.

[26] Wolanski, P. "Opportunities for the Future Turbine Engine with Detonation Combustion Chamber." Prace Instytutu Lotnictwa, Nr 3 (244), s. 202-214, Warszawa (in Polish), 2016.

[27] Kawalec, M. and Wolanski, P. "Research of the Rocket Engine with Detonation Chamber." *26th ICDERS*. Boston, Massachusetts, July 30 – August 4, 2017.

[28] Schwer, D.A. and Kailasanath, K. "Numerical Investigation of Rotating Detonation Engines." *46th Joint Propulsion Conference and Exhibit,* AIAA Paper No. 2014-0284, 2014.

[29] Paxson, D.E. "Numerical Analysis of a Rotating Detonation Engine in the Relative Reference Frame." *52nd AIAA Aerospace Sciences Meeting,* AIAA 2014-0284, 2014.

[30] Kaemming, T., Fotia, M.L., Hoke, J., Schauer, F. "Thermodynamic Modeling of a Rotating Detonation Engine Through a Reduced-Order Approach." *Journal of Propulsion and Power* Vol. 33, No. 5 (September-October 2017).

[31] Kailsanath, K. and Schwer, D.A. "High-Fidelity Simulations of Pressure-Gain Combustion Devices Based on Detonations." *Journal of Propulsion and Power* Vol. 33, No. 1, January-February 2017.

[32] Nordeen, C., Schwer, D., Corrigan, A., and Cetegen, B. "Radial Effects on Rotating Detonation Engine Swirl." *AIAA Propulsion and Energy Forum.* AIAA 6.2015-3781, Orlando, FL, July 27-29, 2015.

[33] Welch, C., Depperschmidt, D., Miller, R., Tobias, J., Uddi, M., and Agrawal, A.K. "Experimental Analysis of Wave Propagation in Methane-Fueled Rotating Detonation Combustor." *Proceedings of ASME TurboExpo 2018.* ASME GT2018-77258, Oslo, Norway, June 11-15, 2018. DOI: 10.1115/GT2018-77258.

[34] Tobias, J., Depperschmidt, D., Miller, R., Uddi, M., and Agrawal, A.K. "OH* Chemiluminescence Imaging of the Combustion Products from a Methane-Fueled Rotating Detonation Engine." *Journal of Engineering for Gas Turbines and Power*, Vol. 141, Issue 2 (2019).

[35] Depperschmidt, D., Tobias, J., Miller, R., Uddi, M., Agrawal, A.K., and Stout, J.B. "Time-Resolved PIV Diagnostics to Measure Flow Field Exiting Methane-Fueled Rotating Detonation Combustor." *AIAA SciTech Forum*. AIAA 62019-1514. San Diego, California, January 7-11, 2019. DOI: 10.2514/6.2019-1514.

[36] Nordeen, C. "Thermodynamics of a Rotating Deontation Engine." Doctoral Dissertation 277. University of Connecticut, Mansfield, CT. 2013.

[37] Raffel, Ma., Willert, C.E., Wereley, S.T., and Kompenhans, J. "Particle Image Velocimetry: A Practical Guide," 2nd Edition, Springer-Verlag Berlin Heidleberg, 2007.

[38] Schröder, A. and Willert, C.E., "Topics in Applied Physics: Particle Image Velocimetry, New Developments and Recent Applications," Vol. 112, Springer-Verlag Berlin Heidelberg, 2008.

[39] Adrian, Ronald J. "Twenty years of particle image velocimetry." *Experiments in Fluids* Vol. 39 (2005): pp 159-169.

[40] Ragni, D., Schrijer, F., van Oudheusden, B.W., and Scarano, F. "Particle Tracer Response Across Shocks Measured by PIV." *Experiments in Fluids* Vol. 50, Issue 1 (2011): pp 53-64.

[41] Rezay Haghdoost, M., Förster, J., Edgington-Mitchell, D., and Oberleithner, K. "Experimental Investigation of Solid Tracer Particle Response Across a Mach Disk by PIV and Schlieren," *International Symposium on Applications of Laser and Imaging Techniques to Fluid Mechanics*. Lisbon, Portugal, July 16-19, 2018.

[42] Opalski, A.B., Paxson, D.E., and Wernet, M.P. "Detonation Driven Ejector Exhaust Flow Characterization Using Planar DPIV." *41st AIAA/ASME/SAE/ASEE Joint Propulsion Conference and Exhibit*. AIAA 2005-4379. Tucson, Arizona. July 10-13, 2005.

[43] Rezay Haghdoost, M., Edgington-Mitchell, D., Paschereit, Ch.O., and Oberliethner, K. "Investigation of the Exhaust Flow of a Pulse Detonation Combustor at different Operating Conditions based on High-Speed Schlieren and PIV." *AIAA SciTech Forum.* AIAA 6.2019-1512. San Diego, California. January 7-11, 2019.

